Instability of a planar expansion wave

A. L. Velikovich,[1] S. T. Zalesak,[1] N. Metzler,[2] and J. G. Wouchuk[3]
[1]*Plasma Physics Division, Naval Research Laboratory, Washington, DC 20375, USA*
[2]*Science Applications International Corporation, McLean, Virginia 22150, USA and NRCN, P.O. Box 9001, Beer Sheva, Israel*
[3]*E. T. S. I. Industriales, Universidad de Castilla-La Mancha, 13071 Cuidad Real, Spain*
(Received 18 March 2005; published 11 October 2005)

An expansion wave is produced when an incident shock wave interacts with a surface separating a fluid from a vacuum. Such an interaction starts the feedout process that transfers perturbations from the rippled inner (rear) to the outer (front) surface of a target in inertial confinement fusion. Being essentially a standing sonic wave superimposed on a centered expansion wave, a rippled expansion wave in an ideal gas, like a rippled shock wave, typically produces decaying oscillations of all fluid variables. Its behavior, however, is different at large and small values of the adiabatic exponent γ. At $\gamma>3$, the mass modulation amplitude δm in a rippled expansion wave exhibits a power-law growth with time $\propto t^{\beta}$, where $\beta=(\gamma-3)/(\gamma-1)$. This is the only example of a hydrodynamic instability whose law of growth, dependent on the equation of state, is expressed in a closed analytical form. The growth is shown to be driven by a physical mechanism similar to that of a classical Richtmyer-Meshkov instability. In the opposite extreme $\gamma-1\ll 1$, δm exhibits oscillatory growth, approximately linear with time, until it reaches its peak value $\sim(\gamma-1)^{-1/2}$, and then starts to decrease. The mechanism driving the growth is the same as that of Vishniac's instability of a blast wave in a gas with low γ. Exact analytical expressions for the growth rates are derived for both cases and favorably compared to hydrodynamic simulation results.

DOI: 10.1103/PhysRevE.72.046306 PACS number(s): 47.20.−k, 47.40.−x, 52.57.Fg

I. INTRODUCTION

Linear stability analysis of rippled centered rarefaction waves has been performed in recent years in connection with the studies of the classical Richtmyer-Meshkov (RM) instability, reflected rarefaction case [1–4]. Rippled rarefaction waves were found to be unstable. Instability of a reflected rippled rarefaction wave produced in a shock-interface interaction is manifested in the linear growth of the ripple amplitude at its trailing edge [2–4]. The ripple amplitude of its leading edge remains constant in time. The unstable trailing edge of a rippled rarefaction wave is a weak discontinuity: The density gradient is discontinuous there. This is why this instability of a rippled rarefaction wave in some sense also turns out to be weak: The linear growth of its trailing edge displacement does not translate into a similar growth of, say, observable mass modulation amplitude $\delta m=\delta\int\rho dx$. As first shown in [3], for ideal gases with moderate values of γ, like $\frac{5}{3}$ or $\frac{7}{5}$, δm in a rippled rarefaction wave exhibits decaying oscillations.

An expansion wave is a rarefaction wave in which a gas rarefies to zero pressure, expanding into vacuum. Such an expansion wave is produced in the limiting case of a heavy-to-light shock-interface interaction, when the density of the light fluid tends to zero. This case is of interest for inertial confinement fusion (ICF) studies because of its relevance to the so-called feedout process that transfers mass perturbations from the inner (rear) to the outer (front) surface of a laser-or hohlraum-driven target, producing a seed for Rayleigh-Taylor (RT) growth [5–10]. Since the small RT seeds contributed by the outer and inner surface roughness and the drive nonuniformity are statistically independent, each of these contributions could be studied separately, one Fourier-Legendre mode at a time. Focusing on the contribution of the inner surface roughness, consider a smooth shock wave that arrives from the uniformly irradiated outer surface of the target and breaks out at its rippled inner surface. Then a rippled reflected rarefaction wave starts propagating back to the outer surface, bringing mass perturbations there. When a spherical target is empty, or filled with a gas whose density is much less than the density of its shell, or if a planar target in vacuum with ripples on its rear surface is used to study feedout, as in the experiments [7,8,10], then the wave reflected from the inner (rear) surface of the target is a rippled expansion wave. The limiting transition from a heavy-to-light case of RM instability to the feedout situation when there is no light fluid behind the rippled surface reached by the shock wave is discussed in detail in [9].

As the pressure behind the trailing edge of a rarefaction wave tends to zero, the growth rate of its instability vanishes [3,4]. Indeed, the fluid particles initially located at the free rear surface of the target, after the shock interaction with this surface, form the expansion front. In planar geometry, normal velocity of the expansion front is the same for its peaks and valleys, $2a_s/(\gamma-1)$, where a_s is the speed of sound behind the incident shock wave. Therefore, the displacement amplitudes of both the leading and the trailing edges of a planar expansion wave are constant in time, and in this sense a rippled expansion wave is stable for any γ.

Surprisingly, it was found in [9] that for $\gamma>3$ the mass modulation amplitude δm in a rippled expansion wave appears to exhibit an unlimited power-law growth. In the opposite limiting case, for γ close to unity, δm is an oscillating function of time, whose amplitude is also found to grow,

linearly with time, until it reaches some peak value. This new instability, developing inside a rippled expansion wave bounded by stable leading and trailing edges, is thus unrelated to the instability of rippled rarefaction waves discussed previously [2–4]. These findings could not be fully understood at the time because the physical mechanisms driving this instability remained unknown, and no formulas were available for its growth rate. Where does this new instability come from?

We report here the solution of this problem. We have explained the physical mechanisms driving the instability, derived explicit asymptotic expressions for the growth rates (Sec. II), and favorably compared our theoretical predictions to 2D numerical simulation results (Sec. III). In Sec. IV we conclude with a discussion.

II. THEORY

Let a planar slab of thickness L be filled with a cold uniform ideal gas, with a single-mode ripple at the rear surface separating the gas from vacuum:

$$\rho(x,y,t\to-\infty)=\begin{cases}0, & x<-L;\\ \rho_0, & -L\leqslant x\leqslant \delta x_0\cos ky;\\ 0, & x>\delta x_0\cos ky,\end{cases} \tag{1}$$

where $k=2\pi/\lambda$ is the ripple wave number. We assume the ripples to be small ($k\delta x_0\ll 1$) and the slab to be thick ($kL\gg 1$) compared to the ripple wavelength λ. The former condition allows us to use the linearized small-amplitude theory. Due to the latter condition, we can follow the evolution of an isolated rippled expansion wave launched at the rear surface of the slab for an arbitrarily long time before its leading edge breaks out at the front surface. Mass modulation amplitude defined as

$$\delta m(t)=\delta\int_{-\infty}^{+\infty}\rho dx=\int_{-\infty}^{+\infty}\delta\rho dx$$
$$=\frac{1}{2}\int_{-\infty}^{+\infty}[\rho(x,y=0,t)-\rho(x,y=\lambda/2,t)]dx \tag{2}$$

is the integral measure of mass perturbation in the slab, which is directly observable in face-on x-ray radiographic images in ICF-related experiments [7,10]. Substituting (1) into (2), we find the initial value of mass modulation amplitude: $\delta m_0=\rho_0\delta x_0$, the initial density times the initial ripple amplitude.

Let a constant pressure p_s be applied at $t=t_1$ to the front surface of the slab. It launches a strong planar shock wave whose front velocity, mass velocity, and the postshock speed of sound are, respectively,

$$D=\left(\frac{(\gamma+1)p_s}{2\rho_0}\right)^{1/2},\quad U=\frac{2}{\gamma+1}D,\quad a_s=\frac{[2\gamma(\gamma-1)]^{1/2}}{\gamma+1}D. \tag{3}$$

Taking $t_1=-L/D$, we make the shock wave arrive at the rear surface of the slab at $t=0$. Obviously, at $t<0$ the mass modulation amplitude is constant, $\delta m=\delta m_0$, because only the initial ripples at the rear surface of the slab contribute to the integral (2). At $t=0$, the planar shock wave breaks out at the rippled rear surface of the slab, instantly producing a rippled expansion wave that propagates from the rear surface into the shocked gas. The reflected expansion wave is bounded by its rippled leading edge and the expansion front, whose ripple amplitudes are, respectively,

$$\delta x_l=\frac{1}{\gamma+1}\{\gamma-1+[2\gamma(\gamma-1)]^{1/2}\}\delta x_0,$$
$$\delta x_e=\frac{1}{\gamma+1}\left[\gamma-1-2\left(\frac{2\gamma}{\gamma-1}\right)^{1/2}\right]\delta x_0; \tag{4}$$

they remain constant in time, see [9]. Starting from $t=0$, the mass modulation amplitude begins to change.

In what follows, we use normalized time

$$\tau=ka_st=\frac{2\pi x_l}{\lambda}, \tag{5}$$

where x_l is the distance traveled by the leading edge of the expansion wave in the shocked gas. The mass modulation amplitude δm will be expressed below in units of δm_0, so that $\delta m(\tau=0)=1$. An exact expression for $\delta m(\tau)$ as a Taylor series in τ had been obtained in [9]. We present it here in a slightly modified form:

$$\delta m(\tau)=2(3-\gamma)\sum_{j=0}^{\infty}\frac{1}{j!}\left[\left(\frac{\gamma+1}{\gamma-3}\right)\frac{\tau^2}{4}\right]^j\times\frac{\{2j[\gamma-1+\sqrt{2\gamma(\gamma-1)}]+\gamma+1\}\Gamma\left[\frac{2(\gamma-1)}{3-\gamma}j+\frac{3}{2}\right]}{[(\gamma-1)j+1]\{4[(\gamma-1)j+1]^2-(\gamma-1)^2\}\Gamma\left[\frac{\gamma+1}{3-\gamma}j+\frac{1}{2}\right]}. \tag{6}$$

The infinite series (6) converges for any finite τ, at any $\gamma>1$, thus generating an entire analytic function of complex variable τ. Retaining a sufficient number of terms in the series, we can follow the evolution of mass modulation amplitude for any finite time $\tau\geqslant 0$. Some examples are shown in Fig. 1.

Observe a somewhat different behavior for moderate (a), large (b), and small (c) values of γ. For the moderate γ case

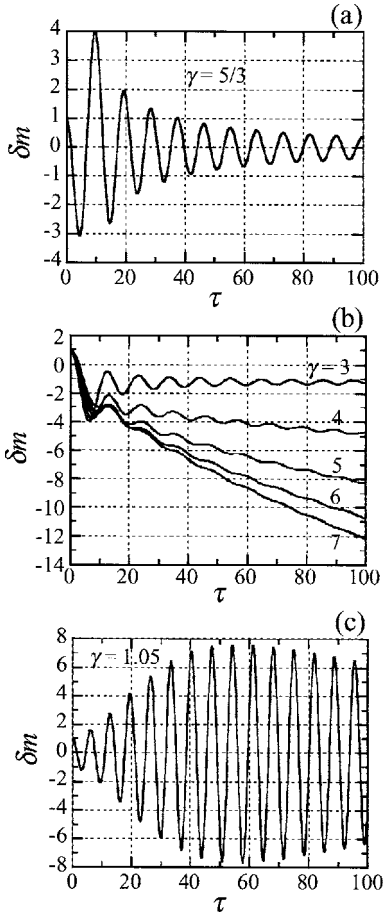

FIG. 1. Time histories of areal mass variation in a rippled expansion wave for moderate $\gamma=\frac{5}{3}$ (a), large $\gamma=3$ to 7 (b), and small $\gamma=1.05$ (c).

of Fig. 1(a), δm rapidly changes phase, as experimentally observed in [10], and then continues to oscillate. Amplitudes of the first several peaks of δm exceed its initial value δm_0 by a factor of 3–4; later, the oscillations decay. For a large γ [Fig. 1(b)], we notice a monotonic growth of δm superimposed on the oscillations: at $\gamma=3$, δm does not seem to decay with time, whereas at $\gamma>3$ the growth appears to be unlimited. For a small γ [Fig. 1(c)], the oscillation amplitude is seen to grow for a longer time than in Fig. 1(a), and reach higher peak values, exceeding δm_0 by an order of magnitude or more, before the oscillations start to decay.

Of course, the time histories shown in Fig. 1 do not constitute a proof of either the decay of oscillations of δm in Figs. 1(a) and 1(c) or of the unlimited growth of δm in Fig. 1(b). At some later time, not shown in the figures, the decay might give way to growth, and vice versa. To make an unambiguous conclusion, one needs to determine the exact asymptotic behavior of the analytic function generated by the series (6) in the limits $\tau\to\infty$, finite $\gamma-1$, and $\gamma-1\to 0$, finite τ, which is done below in this section. Once the asymptotics of δm are established, we need to understand them qualitatively: If there is an instability, we have to explain what physical mechanism drives it.

A. Power-law growth and oscillations at $\gamma=(3n-1)/(n+1)$ and $\gamma\to 1$

At certain values of γ, the asymptotic formulas for $\delta m(\tau)$ in the limit $\tau\to\infty$ could be derived directly from Eq. (6). To do this, we observe that in some particular cases the right-hand side of Eq. (6) reduces to a Taylor expansion of a generalized hypergeometric function. For example, substituting $\gamma=\frac{5}{3}$ into (6), we reduce it to

$$\delta m(\tau) = {}_3F_4\left(1,\frac{3}{2},\frac{3}{2};3,\frac{5}{2},\frac{3}{4},\frac{1}{4};-\frac{\tau^2}{8}\right) - \frac{(\sqrt{5}+1)\tau^2}{10}\,{}_3F_4\left(2,\frac{5}{2},\frac{5}{2};4,\frac{7}{4},\frac{7}{2},\frac{5}{4};-\frac{\tau^2}{8}\right). \quad (7)$$

Such reduction turns out to be possible for an infinite number of values of γ, which satisfy the requirement that the value of the parameter n introduced in [1,4]:

$$n=\frac{\gamma+1}{3-\gamma} \quad (8)$$

is an integer. Positive values of $n\geqslant 1$ generate $\gamma=(3n-1)/(n+1)$ between 1 and 3: 1, $\frac{5}{3}$, 2, $\frac{11}{5}$, … . Negative values of $n\leqslant -2$ generate γ's between 7 and 3: 7, 5, $\frac{13}{3}$, 4,… . For positive $n\geqslant 2$ the analytic function generated by the series (6) is

$$\delta m(\tau) = {}_{n+1}F_{n+2}\left(\frac{1}{n-1},\frac{n+1}{2(n-1)},\frac{3}{2(n-1)},\ldots,\frac{2n-1}{2(n-1)};\frac{2n-1}{n-1},\frac{3n-1}{2(n-1)},\frac{1}{2n},\ldots,\frac{2n-1}{2n};-\frac{1}{4}\left(\frac{n-1}{n}\right)^{n-1}\tau^2\right) - \frac{(n+1)(\sqrt{(3n-1)(n-1)}+n-1)\tau^2}{2(2n-1)(3n-1)}\,{}_{n+1}F_{n+2}\left(\frac{n}{n-1},\frac{3n-1}{2(n-1)},\frac{3}{2(n-1)}+1,\ldots,\frac{2n-1}{2(n-1)}+1;\frac{3n-2}{n-1},\frac{5n-3}{2(n-1)},\frac{1}{2n}+1,\ldots,\frac{2n-1}{2n}+1;-\frac{1}{4}\left(\frac{n-1}{n}\right)^{n-1}\tau^2\right). \quad (9)$$

For negative $n\leqslant -2$

$$\delta m(\tau) = {}_{2-n}F_{3-n}\left(\frac{1}{n-1}, \frac{n+1}{2(n-1)}, -\frac{1}{2n}, \ldots, \frac{2n+1}{2n}; \frac{1}{2(n-1)}, \frac{2n-1}{n-1}, \frac{3n-1}{2(n-1)}, -\frac{1}{2(n-1)}, \ldots, \frac{2n+1}{2(n-1)}; -\frac{1}{4}\left(\frac{n-1}{n}\right)^{n-1}\tau^2\right)$$
$$+ \frac{(n+1)(\sqrt{(3n-1)(n-1)}-n+1)\tau^2}{2(2n-1)(3n-1)} {}_{2-n}F_{3-n}\left(\frac{n}{n-1}, \frac{3n-1}{2(n-1)}, -\frac{1}{2n}+1, \ldots, \frac{2n+1}{2n}+1; \frac{2n-1}{2(n-1)}, \frac{3n-2}{n-1}, \frac{5n-3}{2(n-1)},\right.$$
$$\left. -\frac{1}{2(n-1)}+1, \ldots, \frac{2n+1}{2(n-1)}+1; -\frac{1}{4}\left(\frac{n-1}{n}\right)^{n-1}\tau^2\right). \tag{10}$$

If negative n is an even number, then one upper index $[(n+1)/2(n-1)$ in the first hypergeometric function] coincides with one of the lower indices, reducing the order of the hypergeometric function to ${}_{1-n}F_{2-n}$.

The advantage of the explicit expressions (7), (9), and (10) is that we can readily apply the known formulas for the asymptotic expansions of the generalized hypergeometric functions at large negative argument [11]:

$${}_pF_{p+1}(a_1, \ldots, a_p; b_1, \ldots, b_{p+1}; -z^2)$$
$$\cong \frac{\prod_{j=1}^{p+1}\Gamma(b_j)}{\prod_{k=1}^{p}\Gamma(a_k)}\left(\frac{z^{2\chi}}{\sqrt{\pi}}\cos(2z+\pi\chi)\right.$$
$$\left. + \sum_{i=1}^{p}\Gamma(a_i)\frac{\prod_{k=1,k\neq i}^{p}\Gamma(a_k-a_i)}{\prod_{j=1}^{p+1}\Gamma(b_j-a_i)}z^{-2a_i}\right) \tag{11}$$

at $z\to\infty$, where $\chi=\frac{1}{2}(\Sigma_{k=1}^{p}a_k-\Sigma_{j=1}^{p+1}b_j+\frac{1}{2})$, and a_i, $i=1,\ldots,p$, b_j, $j=1,\ldots,p+1$ are supposed to satisfy the condition that none of a_i, b_j, b_j-a_i, a_k-a_i is zero or a negative integer for any $i,k=1,\ldots,p$, $j=1,\ldots,p+1$, $k\neq i$. Inspecting Eqs. (9) and (10), we find only one such case, when a_i-a_k is zero: in (9), if n is even, $a_2=a_{n/2+1}$. Modification of (11) for this case is done via a limiting transition $a_{n/2+1}\to a_2$ and yields two terms in this sum, one proportional to z^{-2a_2} and another proportional to $z^{-2a_2}\ln z$, which is to be expected in the case of degeneracy. We will not need the explicit form of these terms because they are never dominant in the modified sum (11). Indeed, $a_2=a_1+1/2>a_1$. Since

$$a_1 = \frac{1}{n-1} = \frac{3-\gamma}{2(\gamma-1)} \tag{12}$$

is the lowest of all a_j in both cases (9) and (10), we note that for the hypergeometric functions in (9) and (10), z^{-2a_1} always is the leading power-law term in (11). Substituting the values of indices from (9) and (10) into (11), we find that the main contribution to the oscillating term [from the second terms in the right-hand sides of Eqs. (9) and (10)] is determined by $\chi=-\frac{3}{2}$ for any n. Using the Gauss' multiplication formulas ([12], Eq. 6.1.20) to simplify the products of gamma functions, and expressing the integer n via the adiabatic exponent γ in the final results with the aid of (8), we reduce the leading terms of the asymptotic formula for δm at $\tau\to\infty$ to the following sum:

$$\delta m(\tau) \cong \delta m_{\mathrm{osc}}(\tau) + \delta m_{\mathrm{sec}}(\tau). \tag{13}$$

The dominant oscillatory contribution coming from the leading cosine term in (11) for any γ is given by

$$\delta m_{\mathrm{osc}}(\tau) \cong \frac{4\sqrt{2}[\gamma-1+\sqrt{2\gamma(\gamma-1)}]\sin\Omega\tau}{(\gamma-1)^2\Omega\tau},$$
$$\text{where } \Omega = \left[\frac{2(\gamma-1)}{\gamma-1}\right]^{(\gamma-1)/(3-\gamma)} \tag{14}$$

in agreement with [9].

The dominant monotonic (secular) contribution coming from the leading power-law term in (11) for $\gamma<3$ describes power-law decay

$$\delta m_{\mathrm{sec}}(\tau) \cong -\frac{2\sin\left(\frac{\pi}{\gamma-1}\right)}{(\gamma-1)^4}\left[2(\gamma-1)^2+(\gamma-3)\sqrt{2\gamma(\gamma-1)}\right]$$
$$\times\Gamma\left(\frac{2}{\gamma-1}\right)\left(\frac{\gamma+1}{3-\gamma}\tau^2\right)^{(\gamma-3)/2(\gamma-1)}, \tag{15}$$

whereas for $\gamma>3$ it describes power-law growth

$$\delta m_{\mathrm{sec}}(\tau) \cong -\frac{2}{(\gamma-1)^4}\left[2(\gamma-1)^2+(\gamma-3)\sqrt{2\gamma(\gamma-1)}\right]$$
$$\times\Gamma\left(\frac{2}{\gamma-1}\right)\left(\frac{\gamma+1}{\gamma-3}\tau^2\right)^{(\gamma-3)/2(\gamma-1)}. \tag{16}$$

Of course, (15) represents a branch of the same analytic function of τ as (16). As $\gamma-3$ changes sign, the noninteger power of negative $(\gamma+1)\tau^2/(\gamma-3)$ in (16) becomes a complex-valued function. The right-hand side of (15) gives the real part of this complex function for one of its branches. The other branches would produce phase shift factors $(-1)^s\sin[(2s+1)\pi/(\gamma-1)]$, where s is an arbitrary integer number; the branch (15) corresponds to $s=0$, the phase shift factor being $\sin[\pi/(\gamma-1)]$.

The exact asymptotic expressions (14)–(16) have been derived above only for a discrete set of γ's given by (8). Since this is an infinite set with an accumulation point, one can reasonably expect these formulas to be valid for an arbitrary $\gamma>1$, if the asymptotic expressions sought for are analytic functions of the parameter γ and pertain to the same sheet of the Riemann surface. A rigorous derivation of (16) in the next section confirms that this is indeed the case.

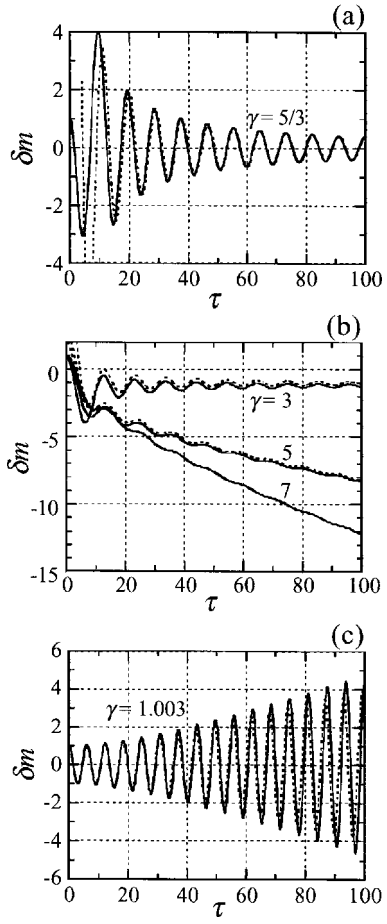

FIG. 2. Exact (solid) and asymptotic (dotted lines) time histories of areal mass variation in a rippled expansion wave for $\gamma=\frac{5}{3}$ (a), $\gamma=3$ to 7 (b), and $\gamma=1.003$ (c).

Asymptotic formulas (14)–(16) describe oscillatory decay and power-law secular growth of δm at large τ for $\gamma<3$ and $\gamma>3$, respectively. For $\gamma=3$ mass modulation amplitude at large τ tends to a constant value, exactly equal to its initial value but with inverted phase. Taking the limit $\gamma\to 3$ in (15) or (16), we find

$$\delta m(\tau) \cong -1 + \frac{2\sqrt{2}(\sqrt{3}+1)\exp\left(\frac{1}{2}\right)}{\tau} \sin\left[\exp\left(-\frac{1}{2}\right)\tau\right]. \tag{17}$$

Oscillations (14) decay as $1/\tau$, the monotonic term (15)—as τ^{β}, where

$$\beta = \frac{\gamma-3}{\gamma-1}. \tag{18}$$

For $\gamma<2$ we have $\beta<-1$, and therefore the oscillatory decay of δm at large τ (14) dominates over the monotonic decay (15). For $2<\gamma<3$ the reverse is true.

In Figs. 2(a) and 2(b), we compare the asymptotic solution (13) with the exact solution (6) at finite times for moderate and large γ. The agreement at large τ is good, as it should be.

Now consider the limit of small $\gamma-1\to 0$. The limiting value $\gamma=1$ corresponds to the value of $n=1$ in (8), for which the series (6) reduces to $\cos\tau$. Expanding the coefficients of the series (6) into a power series near $\gamma=1$, we obtain the next term in the asymptotic expansion of δm in the limit $\gamma-1\to 0$, finite τ:

$$\delta m(\tau) \cong \cos\tau - \left(\frac{\gamma-1}{2}\right)^{1/2} \tau \sin\tau. \tag{19}$$

This formula describes oscillations whose amplitude grows linearly with time. Matching (19) to the asymptotic expression (14) valid for large τ, we estimate the time when $\delta m(\tau)$ reaches its peak as

$$\tau_{\text{peak}} \cong 2^{7/4}(\gamma-1)^{-1}. \tag{20}$$

Substituting this into (19), we obtain a rough estimate for the peak value of mass modulation amplitude

$$\delta m_{\text{peak}} \cong 2^{5/4}(\gamma-1)^{-1/2}. \tag{21}$$

Figure 2(c) compares the asymptotic expression (19) to the exact result (6) for a very small $\gamma=1.003$. The linear growth (19) is seen to be a good approximation for a finite time. For some time, before this oscillatory growth reaches the peak amplitude and evolves into an oscillatory decay, the growth is even faster than Eq. (19) predicts.

The discussion of the physical mechanisms driving the power-law growth (16) and the linear growth (19) will follow in Sec. II C. The next section contains a rigorous derivation of (16) for arbitrary γ.

B. Power-law growth at arbitrary $\gamma>3$

We start with the continuity equation written in the linear approximation for a small single-mode perturbation imposed on a rippled rarefaction wave:

$$\frac{\delta\rho}{\partial t} + \frac{\partial}{\partial x}(\rho v_x) + ik\rho^{(0)} v_y = 0, \tag{22}$$

where $\rho^{(0)}$ stands for the unperturbed gas density in the planar rarefaction wave. With the aid of (22) we find that the areal mass integral (2) satisfies a differential equation

$$\frac{d}{dt}\delta m = -ik\int_{x_l}^{x_t} \rho^{(0)} v_y dx, \tag{23}$$

where x_l and x_t are the coordinates of the leading and the trailing edges of the expansion wave, respectively. We normalize δm in the same way as in (6), define a dimensionless lateral velocity δv_y by $v_y=-ik\delta x_0 a_s\times\delta v_y$, and introduce the normalized speed of sound in the unperturbed expansion wave as $A=a/a_s$. At the leading edge of the expansion wave $A=1$, at its trailing edge $A=0$. The unperturbed density in the expansion wave is expressed via A as $\rho^{(0)}=\rho_s A^{2/(\gamma-1)}$, and $dx=-\alpha a_s t dA$, where $\alpha=(\gamma+1)/(\gamma-1)$ and $\rho_s=\alpha\rho_0$ is the postshock density [3,4]. Substituting these definitions into Eq. (23), we can present the solution of this equation satisfying the initial condition $\delta m(0)=1$ as

$$\delta m(\tau) = 1 - \alpha^2 \int_{+0}^{\tau} \tau' d\tau' \int_0^1 A^{2/(\gamma-1)} \delta v_y(A,\tau') dA. \quad (24)$$

The lateral velocity profile $\delta v_y(A,\tau)$ is known from the linear perturbation analysis of a rippled rarefaction wave [1,4]. For $\gamma > 3$ it is written as

$$\delta v_y(A,\tau) = A^{\beta/2} \int_{A^\beta}^1 dz \, \delta w_1(z) J_0(\tau\phi(A,z)), \quad (25)$$

where β is given by (18), $\phi(A,z) = A^{\alpha/2}\sqrt{n(A^\beta - z)}$, n is given by (8) (note that for arbitrary $\gamma > 3$, β is positive, n is negative, and not necessarily integer), and

$$\delta w_1(z) = \sum_{j=0}^{2} \alpha_j \varepsilon_j z^{\varepsilon_j - 1}; \quad (26)$$

$$\alpha_0 = -\frac{2(\gamma-1)\mathrm{M}_2 + \gamma - 3}{(\gamma-1)^2 R \mathrm{M}_2}, \quad \alpha_1 = 2\frac{(\gamma-1)\mathrm{M}_2 - 2}{(\gamma-1)^2 R \mathrm{M}_2},$$

$$\alpha_2 = \frac{\gamma+1}{(\gamma-1)^2 R \mathrm{M}_2}; \quad (27)$$

$$\varepsilon_j = -\frac{1}{2} + \frac{j}{\beta}, \quad j = 0,1,2. \quad (28)$$

Here $\mathrm{M}_2 = (D-U)/a_s < 1$ is the downstream Mach number of the incident shock wave, $R = D/(D-U) > 1$ is the density compression ratio; in the strong-shock limit $\mathrm{M}_2 \to \sqrt{(\gamma-1)/(2\gamma)}$, $R \to (\gamma+1)/(\gamma-1)$ [see (3)]. The function δw_1 characterizes the initial profile of lateral velocity δv_y produced when the rippled expansion wave was formed in the interaction of the planar incident shock wave with a rippled free rear surface at $\tau \to +0$ [1,3,4]. Formulas (25)–(28) are valid for a rippled rarefaction wave produced by a shock wave of arbitrary strength interacting with a material interface with arbitrary density ratio. For $\gamma < 3$ we have $\beta < 0$, so $A^\beta > 1$, and integration in (25) goes from 1 to A^β.

One is tempted to find the asymptotic expression for $\delta m(\tau)$ at $\tau \to \infty$ by simply substituting the asymptotic expression for Bessel function $J_0(\tau\phi)$ at large argument into (25) and then performing the integrations. This approach, however, would lead to incorrect results: the asymptotic of a sum is not equal to the sum of the asymptotics. Physically, we have to perform integration over standing sonic waves whose oscillation frequencies are slightly different. When summed up, the phase shifts between them turn out to be important enough to drastically change the asymptotic character of the result. Therefore we need a different strategy.

Let us substitute (25) into (24) and simplify the result using the identity $zJ_0(z) = (d/dz)[zJ_1(z)]$ ([12], Eq. 9.1.30) to integrate over τ':

$$\delta m(\tau) = 1 - \alpha^2 \tau^2 \int_0^1 A^{\alpha/2} dA \int_{A^\beta}^1 dz \, \delta w_1(z) \frac{J_1(\tau\phi(A,z))}{\tau\phi(A,z)}$$

$$= 1 - \alpha^2 \tau^2 \sum_{j=0}^{2} \alpha_j \varepsilon_j Q_j(\tau), \quad (29)$$

where

$$Q_j(\tau) = \int_0^1 A^{\alpha/2} dA \int_{A^\beta}^1 dz z^{\varepsilon_j - 1} \frac{J_1(\tau\phi(A,z))}{\tau\phi(A,z)}$$

$$= \frac{1}{2\pi i} \int_{-i\infty}^{+i\infty} d\theta \frac{\Gamma(-\theta)}{\Gamma(2+\theta)} \left(-\frac{n\tau^2}{4}\right)^\theta$$

$$\times \int_0^1 dA A^{\alpha/2 + \alpha\theta} q_j(A,\theta), \quad j = 0,1,2. \quad (30)$$

In (30) we have used integral representation ([12], Eq. 9.1.26) for $J_1(z)$. The integrals over z denoted by $q_j(A,\theta)$ in (30) are expressed via hypergeometric functions ([13], Eqs. 3.197):

$$q_j(A,\theta) = \int_{A^\beta}^1 dz z^{\theta + \varepsilon_j - 1} \left(1 - \frac{A^\beta}{z}\right)^\theta = A^{\beta(\theta+\varepsilon_j)} \frac{(1-A^\beta)^{\theta+1}}{\theta+1}$$

$$\times {}_2F_1(\theta + \varepsilon_j + 1, \theta + 1; \theta + 2; 1 - A^\beta). \quad (31)$$

This explicit expression allows one to perform the integration over A in (30). The result is

$$Q_j(\tau) = \frac{1}{2\beta} \int_{-i\infty}^{+i\infty} \frac{d\theta}{2\pi i} \frac{\Gamma(-\theta)\Gamma\left(\frac{2\alpha\theta + \alpha + 2}{2\beta}\right)}{\Gamma\left(\frac{4\theta + \alpha + 2}{2\beta} + 1\right)}$$

$$\times \frac{\left(-\frac{n\tau^2}{4}\right)^\theta}{(\theta+1)\left(\frac{4\theta+\alpha+2}{2\beta} + \varepsilon_j\right)}. \quad (32)$$

We are interested in the asymptotic behavior of $Q_j(\tau)$ at $\tau \to \infty$. The asymptotic expressions sought for are obtained by closing the integration contour on the complex plane θ to the left side and calculating the residues contributed by the poles at negative real values of θ. These are zeroes of the denominator, $\theta = -1$ and

$$\theta_j = -\frac{1}{2} - \frac{\alpha}{4} - \frac{\beta}{2}\varepsilon_j = -\frac{1}{2}(j + \alpha), \quad j = 0,1,2, \quad (33)$$

and the poles of the Gamma function in the numerator,

$$\Theta_l = -\frac{1}{2} - \frac{1}{\alpha} - \frac{\beta}{\alpha} l, \quad l = 0,1,2,\ldots. \quad (34)$$

After some algebra, we find the asymptotic expansions of $Q_j(\tau)$ in powers of τ, which for (29) translate into

$$\delta m(\tau) \cong -\frac{\beta}{2} - \frac{\alpha^2}{4}\sum_{j=0}^{2}\alpha_j\varepsilon_j\left[\frac{\Gamma(-\theta_j)\Gamma\left(\frac{2\alpha\theta_j+\alpha+2}{2\beta}\right)}{(\theta_j+1)\Gamma\left(\frac{4\theta_j+\alpha+2}{2\beta}+1\right)}\left(-\frac{n}{4}\right)^{\theta_j}\tau^{\beta-j}\right.$$

$$\left.+\sum_{l=0}^{\infty}\frac{(-1)^l\Gamma(-\Theta_l)}{l!(\Theta_l+1)\Gamma\left(\frac{4\Theta_l+\alpha+2}{2\beta}+1\right)\left(\frac{4\Theta_l+\alpha+2}{2\beta}+\varepsilon_j\right)}\left(-\frac{n}{4}\right)^{\Theta_l}\tau^{(2l+1)/n}\right] \text{ at } \tau\to\infty. \quad (35)$$

Since for $\gamma>3$ we have $0<\beta<1$ and $n<0$, the only term on the right-hand side of Eq. (35) that grows at $\tau\to\infty$ is the first $j=0$ term in the square brackets. Substituting (28) and (33) into this term, and using the duplication formula ([12], Eq. 6.1.18) to simplify the product of two gamma functions in the numerator, we transform it into

$$\delta m(\tau) \cong \alpha\alpha_0\Gamma(\alpha)\left(\frac{\gamma+1}{\gamma-3}\right)^{\beta/2}\tau^{\beta} \text{ at } \tau\to\infty. \quad (36)$$

This is identical to (16). Validity of the asymptotic expression (16) for arbitrary $\gamma>3$ has thus been proved. Since the γ-dependent coefficient in (15) represents a branch of the same analytic function of γ, and it has been checked in Sec. II A that for all $\gamma<3$ satisfying (8) the corresponding coefficients belong to the same sheet of the Riemann surface, we conclude that (15) is also valid for arbitrary γ between 1 and 3. A similar argument applies to (14).

C. Qualitative discussion

The physical mechanism of unbounded perturbation growth at $\gamma>3$ is somewhat similar to that of classical RM instability. In the RM case, the fluid near a material interface gets initial kick when the incident planar shock wave interacts with it. During the short time interval of shock-interface interaction, a finite surface vorticity is deposited at the shocked rippled interface, and this vorticity essentially drives the subsequent linear RM growth.

Although the flow in a rarefaction wave propagating into an unperturbed gas is vorticity-free, the shock-free-rippled-surface interaction produces a finite, constant in time lateral fluid velocity at the trailing edge of the expansion wave, that is, at the expansion front. Taking the limit $A\to 0$ at finite $A\tau$ in (25), we find

$$\delta v_y(A\to 0,\tau) = -\alpha_0\exp(-A\tau\sqrt{-n}). \quad (37)$$

At the expansion front, where $A=0$, we have $\delta v_y=-\alpha_0$ at all time. Of course, at the trailing edge the density $\rho^{(0)}$ vanishes. However, since $\rho^{(0)}=\rho_s A^{2/(\gamma-1)}$, and the power $2/(\gamma-1)$ for $\gamma>3$ is less than unity, normal density gradient $\partial\rho^{(0)}/\partial x$ diverges at the trailing edge, indicating accumulation of mass in its vicinity. On the other hand, both the unperturbed pressure $p^{(0)}=p_s A^{2\gamma/(\gamma-1)}$ and its normal gradient $\partial p^{(0)}/\partial x$ vanish at the trailing edge, which means that mass could be continuously shifted laterally near the trailing edge without building up a substantial counter-pressure that could give rise to sonic oscillations driving the mass back.

Figure 3 shows the profiles of normalized lateral velocity $\delta v_y(\eta,\tau)$ (a) and density modulation $\delta\rho$ [the latter is defined by $\rho=\rho^{(0)}+k\delta x_0\times\delta\rho(\eta,\tau)$] (b) amplitudes versus the dimensionless self-similar coordinate η for $\gamma=5$. Here $\eta=(x-Ut)/a_s t=[2-(\gamma+1)A]/(\gamma-1)$ [3,4]; the leading and the trailing edges of the expansion wave correspond to $\eta=-1$ and $\eta=2/(\gamma-1)$, respectively. At the trailing edge, the lateral velocity maintains its constant maximum value $-\alpha_0$. Some gas particles, which have initially received lateral velocities δv_y close to $-\alpha_0$, continue their ballistic motion in the same direction. If we could assume that the same set of fluid particles has lateral velocities, say, between $-\alpha_0/2$ and $-\alpha_0$ at all times, then the contribution of these particles to δm would be estimated by taking $\delta v_y\approx-\alpha_0$ and integrating over A in (24) from 0 to $A_{\max}=\text{const}\times\tau^{-(\gamma-1)/(\gamma+1)}$ (normalized speed of sound $A(\tau)$ in a given fluid particle in a centered rarefaction wave varies with time as $\tau^{-(\gamma-1)/(\gamma+1)}$, see [3], Eq. (17)).

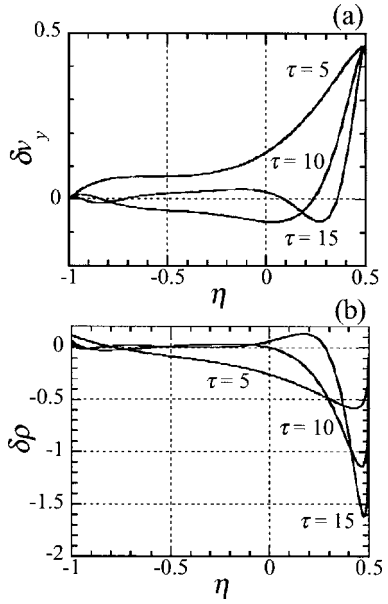

FIG. 3. Profiles of normalized lateral velocity δv_y (a) and density modulation $\delta\rho$ (b) amplitudes versus self-similar coordinate $\eta=(x-Ut)/a_s t$ for $\gamma=5$ at $\tau=5$, 10, and 15.

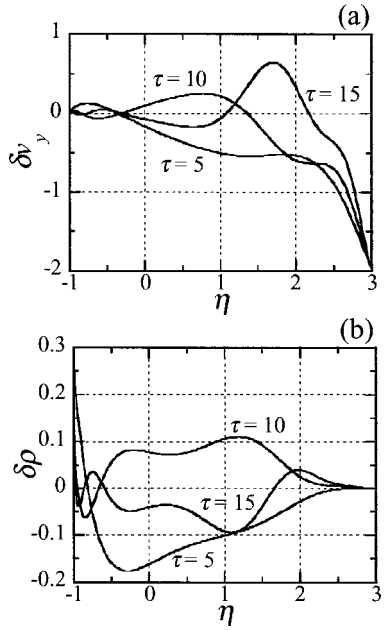

FIG. 4. Same as in Fig. 3 for $\gamma=\frac{5}{3}$.

Not surprisingly, this assumption translates into a linear growth of δm with time—a constant fraction of mass moves laterally with a constant velocity, resulting in a linear growth of mass modulation amplitude. This is basically how the classical RM instability develops.

The difference between the instability of an expansion wave and the classical RM instability is that in the latter case the ballistic fluid flow along the material interface is vortical and, therefore, it is not accompanied with a build-up of a counter-pressure slowing down the lateral motion. On the other hand, the flow in the expansion wave is isoentropic and vorticity-free, hence all our perturbations are sonic waves. Though the gas pressure near the trailing edge is low, it is still gradually slowing down the lateral motion of gas particles. Equation (37) shows that the values of A and τ corresponding to δv_y equal to some sizeable fraction of $-\alpha_0$ are related by $A\tau=$const. It means that, as the lateral fluid motion slows down, the number of particles whose velocities exceed, say, $-\alpha_0/2$, decreases with time as $\tau^{-2/(\gamma+1)}$. Substituting (37) into (24) and calculating the integral in the limit $A \to 0$ at finite $A\tau$, we readily reproduce Eq. (16). The density profiles for this case shown in Fig. 3(b) demonstrate mass accumulation near the trailing edge of the expansion wave.

For comparison, Fig. 4 shows the profiles of lateral velocity and density in a rippled rarefaction wave for a stable case of $\gamma=\frac{5}{3}$. The lateral velocity profiles of Fig. 4(a) are not that different from those shown in Fig. 3(a). The gas mass near the trailing edge is still driven in the lateral direction at almost constant velocity, but now there is little mass there to redistribute, and the fraction of particles whose lateral velocity is close to $-\alpha_0$ decreases so fast that the total contribution of this mechanism to δm decays with time. The density modulation amplitude oscillates, showing no accumulation.

Figure 5 shows the profiles of lateral velocity and density for γ close to unity, $\gamma=1.1$. Here, $\rho^{(0)}$ rapidly decays with increased distance from the leading edge of the expansion

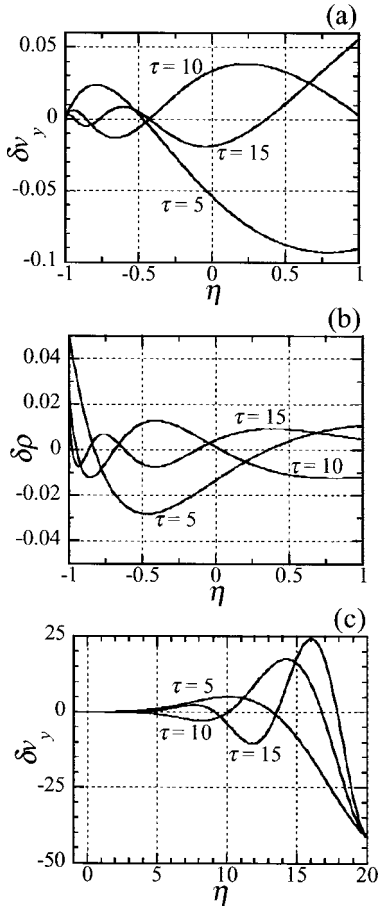

FIG. 5. Same as in Figs. 3 and 4 for $\gamma=1.1$, with profiles (a) and (b) zoomed near the head of the expansion wave, and the profile of δv_y (c) also shown in full.

wave. Therefore, only the gas layer near the leading edge contributes to δm. Just as above, the highest value of δv_y is near the trailing edge, but since there is virtually no mass there, ballistic mass motion near the trailing edge started in the shock-free-rippled-surface interaction adds no contribution to δm. The areal mass is redistributed by the oscillating lateral velocity generated in the vicinity of the rippled leading edge of the expansion wave as a result of lateral pressure gradient.

The physical mechanism of perturbation growth here is essentially the same as in a pendulum oscillating in a decreasing gravitational field. When the pendulum swings from the equilibrium position, the restoring force that decelerates it is less than the force that accelerated it when it approached the equilibrium, hence in each oscillation it deviates farther from the equilibrium [14,15]. Similarly, here the pressure gradient drives the mass laterally until it overshoots the equilibrium, and a comparable counter-pressure builds up. When the gas mass starts moving in the opposite direction, the unperturbed pressure there is already less, and it takes a larger displacement to slow the mass down. Eventually, every fluid particle approaches the trailing edge and the sonic oscillations start to decay according to (14).

The same mechanism drives the so-called Vishniac instability of a blast wave in a gas with low γ [16]. Low values of

ideal gas γ are conventionally used to model dynamics of strongly radiating gases. The accuracy of such approximation is beyond the scope of the present paper (see [17] and references therein). A blast wave consists of a shock wave and a rarefaction wave immediately following it [18]. A planar shock wave in an ideal gas is stable for any γ [19]. When rippled shock and rarefaction waves are coupled, as in the case of a rippled blast wave, the shock wave feeds to the leading edge of the rarefaction wave a nonzero value of lateral velocity δv_y, in contrast with the case of a stand-alone rippled rarefaction wave, where $\delta v_y=0$ at its leading edge, cf. Figs. 3(a), 4(a), and 5(a). Since the rippled shock wave acts both as a source of perturbations and as a stabilizer for the rippled rarefaction wave, all Vishniac perturbation growth is entirely due to the instability of a rippled rarefaction wave at low γ discussed above. If γ is not small enough, $\gamma>1.2$ for planar geometry [16], then there is no instability. Even if γ is sufficiently small, say, $\gamma=1.1$, the growth in a planar geometry occurs only during a finite time interval (cf. Fig. 5(a) of [16]), same as for a rippled expansion wave here [see Fig. 1(c)]. A similar behavior of δm—its oscillatory growth during a finite time interval, which is longer for a lower γ—had been established in [15] for a shock-rarefaction flow produced by an impulsive loading rather than a blast.

Finally, let us discuss how the present results are modified for a finite-strength rarefaction wave, where the normalized speed of sound decreases from $A=1$ not to $A=0$ but to some finite minimum value of $A=\mathrm{M}_1>0$. This corresponds to the unperturbed shock wave incident upon a material interface with large density difference $\rho_{\mathrm{light}}/\rho_{\mathrm{heavy}}\ll 1$ rather than upon a free rear/inner surface. Then there is no unlimited growth of δm because all the impulsively accelerated fluid particles that would have driven the growth in an expansion wave leave the finite-strength rarefaction wave within a finite time interval τ of order of $\mathrm{M}_1^{-(\gamma+1)/(\gamma-1)}$ where

$$\mathrm{M}_1 \approx \left(\frac{2\gamma\rho_{\mathrm{light}}}{(\gamma-1)\rho_{\mathrm{heavy}}}\right)^{(\gamma-1)/2\gamma}. \tag{38}$$

A finite counter-pressure eventually leads to a phase reversal of δm, so that at late time the mass modulation amplitude in a finite strength rippled rarefaction wave oscillates around zero average value for any γ [see Fig. 6(a)]. The growth phase at $\gamma>3$ lasts only a finite time and is only noticeable for low values of M_1 that correspond to very low density ratios $\rho_{\mathrm{light}}/\rho_{\mathrm{heavy}}$. For example, $\mathrm{M}_1=0.01$ in a gas with $\gamma=4$ corresponds to a strong shock interaction with a material interface where the density ratio is $\rho_{\mathrm{light}}/\rho_{\mathrm{heavy}}=1.7\times10^{-6}$.

In contrast with this, in a gas with a low γ the behavior of δm in a finite-strength rarefaction wave does not differ from the case of an expansion wave [see the example shown for $\gamma=1.1$ in Fig. 6(b)]. Here, the curves corresponding to M_1 between 0 and 0.6 are on top of each other, and the effect of finite M_1 is only observable starting from $\mathrm{M}_1=0.7$. This is because the vicinity of the trailing edge plays no role here; the mass redistribution occurs predominantly near the leading edge, where our exact solutions do not depend on M_1 at all. This is why our qualitative arguments are applicable to

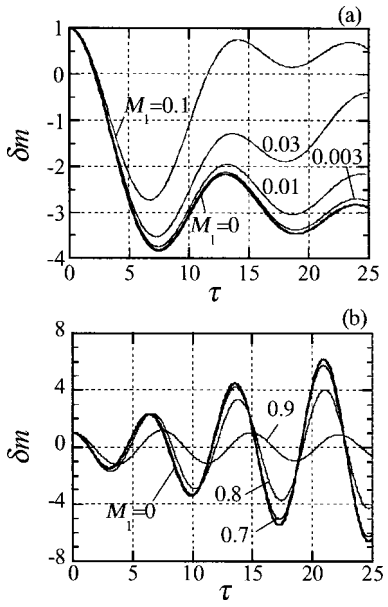

FIG. 6. Time histories of areal mass variation in a rippled rarefaction wave of finite strength, with rarefaction Mach number M_1 varying from 0 (expansion wave limit) to 0.1 for $\gamma=4$ (a) and to 0.9 for $\gamma=1.1$ (b).

the case of a planar blast wave discussed above, where the gas behind the shock wave decompresses to some finite, time-dependent minimal pressure.

III. NUMERICAL SIMULATIONS

The theoretical results discussed in Sec. II are exact, and therefore do not require numerical validation. Rather, they could be helpful for testing the accuracy of our codes in modeling evolution of small perturbations in feedout-related problems. Reproducing these exact theoretical results in a numerical simulation is a challenging task, given the important roles of compressibility, high gradients, and large density differences (in the range of 10^4–10^6 for relevant cases). Another important factor is the smallness of the initial amplitude that ensures linearity. If we take the initial normalized amplitude $k\delta x_0$ too large, the nonlinear effects will be noticeable from the start. On the other hand, small initial amplitudes are notoriously hard to resolve, and there is always a risk either to contaminate the simulation results involving such amplitudes with a numerical noise or to damp them heavily with a numerical dissipation. In real-life situations, we have no choice but to trust the codes; exact solutions help us to test how good they are.

Our simulations were performed in two dimensions using the FAST2D hydrocode developed at the Naval Research Laboratory [20] (more details and further references are given in [14]) and the Sandbox code [21], which had been specifically designed to accurately describe evolution of very small hydrodynamic perturbations. The initial conditions correspond to the instant when a planar shock wave reaches the valleys of a rippled interface separating heavy and light gases. The shock speed is $D=10^7$ cm s^{-1}; the ripple wavelength is $\lambda=15$ μm. Numerical resolution in FAST2D has

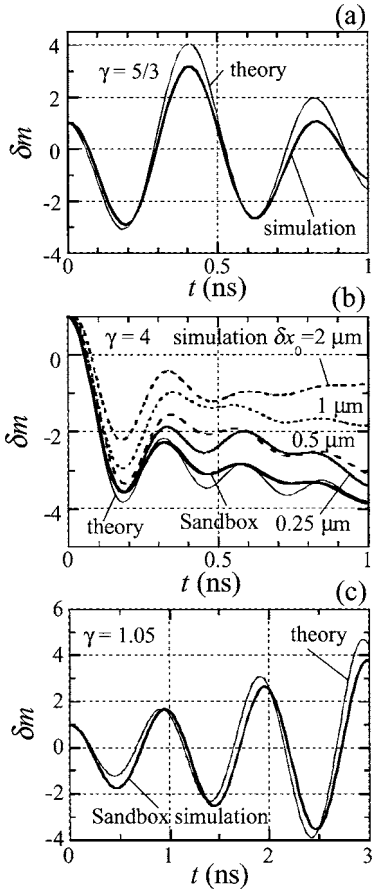

FIG. 7. Simulated (thick solid, dashed, and dotted lines) and exact analytical (thin solid lines) time histories of areal mass variation in a rippled expansion wave for $\gamma=\frac{5}{3}$ and $k\delta x_0=0.1$ (a); $\gamma=4$ and $k\delta x_0$ varied from 2×10^{-6} (Sandbox) to 0.1 to 0.8 (b); and $\gamma=1.05$ and $k\delta x_0=2\times10^{-6}$ (c).

been chosen slightly higher than in our modeling of the experiments on feedout [10] and is arguably adequate to the practical state of the art for simulations like that performed in ICF-related studies. The version of Sandbox used here was a linearized, fully spectral code in the y direction and finite-difference Godunov hydrodynamic code in the x direction.

We start with $\gamma=\frac{5}{3}$, initial ripple amplitude $\delta x_0=0.25$ μm, and density ratio $\rho_{\text{light}}/\rho_{\text{heavy}}=10^{-4}$, which corresponds to $M_1=0.24$. Figure 7(a) demonstrates a good agreement between the theory and FAST2D simulation, particularly in the timing of minima and maxima. The remaining small discrepancy is not explained by a finite value of M_1 (cf. Fig. 6) because for $\gamma=\frac{5}{3}$ the $M_1=0$ and $M_1=0.24$ theoretical curves are much closer to each other than theory and simulation curves in Fig. 7, and small discrepancy between them is seen both near the minima and the maxima. To some extent, the deviation seen in Fig. 7(a) may be due to nonlinearity ($k\delta x_0=0.1$), but most likely it is caused by numerical diffusion.

A similar simulation has been done for $\gamma=4$ and initial ripple amplitude δx_0 varied from 5×10^{-6} (Sandbox) to 0.25 to 2 μm (FAST2D) [Fig. 7(b)]. The same density ratio $\rho_{\text{light}}/\rho_{\text{heavy}}=10^{-4}$ now corresponds to $M_1=0.046$. With the initial amplitude δx_0 decreasing, the simulated time history $\delta m(\tau)$ approaches the theoretical curve, as it should. Comparing Fig. 7(b) to Fig. 6, we see that the simulated curves for $\delta x_0=5\times10^{-6}$ μm and 0.25 μm are actually closer to the theoretical curve for $M_1=0$ than the actual theoretical curve for $M_1=0.046$. Of course, the numerical δm includes contributions from the flow downstream from the trailing edge of the rarefaction wave, which, in addition to numerical diffusion, can slow down the decay of δm with time in comparison to that shown in Fig. 6.

Figure 7(c) presents the results of the Sandbox simulation for $\gamma=1.05$, a lower density ratio $\rho_{\text{light}}/\rho_{\text{heavy}}=10^{-5}$ that now corresponds to $M_1=0.792$, and initial ripple amplitude $\delta x_0=5\times10^{-6}$ μm. The simulation results are in a good agreement with the theoretical prediction of linear growth, as they should be.

IV. CONCLUSIONS

We have studied two kinds of instability of a centered expansion wave. One of them takes place for large $\gamma>3$ and manifests itself in an unlimited monotonic power-law growth of mass variation amplitude with time $\propto t^{\beta}$, where $\beta=(\gamma-3)/(\gamma-1)$. Of course, such large values of $\gamma>3$, while not prohibited thermodynamically, do not approximate the equation of state of any gas or other medium at expansion. Nevertheless, the study of this instability, in our opinion, adds some insight to the general theory of hydrodynamic instabilities. The power index of this new instability is determined by the equation of state, just as for Vishniac's instability of a blast wave, and, in contrast with the latter case, is expressed in a closed analytical form. The physical mechanism driving this instability, however, is entirely different from Vishniac's instability. Rather, it is essentially the same as in classical Richtmyer-Meshkov instability. The instability is driven by a ballistic motion of the fluid in the lateral direction, which is launched by the initial interaction of a smooth incident shock with a rippled rear surface. We can state that this new instability is in a sense an expansion-wave counterpart of the shock-induced classical RM instability. In the RM case, the fluid initially put into the lateral motion continues to slide along the material interface without creating a counterpressure that could slow down its flow, which results in a linear growth of mass variation amplitude δm with time. In an expansion wave, the lateral flow of a fluid is a sonic wave in a gas whose speed of sound in the vicinity of the expansion front approaches but not equals zero. The counterpressure developing in such a sonic wave gradually slows down the fluid particles, removing them from the initially launched lateral flow. Our condition $\gamma>3$ is required to make the contribution of these particles to δm grow faster than the rate at which they are removed. If this condition is satisfied, then the power index β is still less than unity, the power of time characteristic of the classical RM instability, as it should be.

We have also studied another kind of instability which develops for γ close to unity. It is sometimes argued that such values of γ represent reasonable, if crude, approximation of equation of state for strongly radiating gases. This instability develops not only in expansion waves but in rar-

efaction waves of arbitrary strength. It manifests itself in an oscillatory growth of δm, the oscillations amplitude increasing linearly with time. The growth continues for a finite time interval, which is longer for γ closer to unity, until δm reaches a peak value, which is higher for γ closer to unity, and then an oscillatory decay follows. Similar behavior had been demonstrated for Vishniac's instability of a blast wave in planar geometry [16]. In this case, apparent similarity with Vishniac's instability is based on a physical analogy. In our opinion, Vishniac's perturbation growth in a blast wave is driven by exactly the same mechanism as described here, the instability developing in the rarefaction-wave component of a rippled blast wave. Its shock-wave component serves both as a stabilizer and as a source of initial perturbations for the rippled rarefaction wave that follows it in a blast wave, but is not unstable by itself for any γ.

ACKNOWLEDGMENTS

The authors are grateful to A. J. Schmitt, J. H. Gardner, and J. M. Laming for helpful discussions. A.L.V., S.T.Z., and N.M. are supported by the U.S. Department of Energy, Defense Programs, J.W.G. by the Ministry of Educacion y Ciencia (FTN 2003-0072) and Consejo de Comunidades de Castilla-La Mancha, Spain.

[1] Y. Kivity and M. Hanin, Isr. J. Technol. **8**, 139 (1970); Phys. Fluids **24**, 1010 (1981).
[2] Y. Yang, Q. Zhang, and D. H. Sharp, Phys. Fluids **6**, 1856 (1994).
[3] A. L. Velikovich and L. Phillips, Phys. Fluids **8**, 1107 (1996).
[4] J. G. Wouchuk and R. Carretero, Phys. Plasmas **10**, 4237 (2003).
[5] K. O. Mikaelian, Phys. Rev. A **31**, 410 (1985).
[6] R. Betti, V. Lobatchev, and R. L. McCrory, Phys. Rev. Lett. **81**, 5560 (1998).
[7] D. P. Smitherman, R. E. Chrien, N. M. Hoffman, and G. R. Magelssen, Phys. Plasmas **6**, 932 (1999).
[8] K. Shigemori, M. Nakai, H. Azechi, K. Nishihara, R. Ishizaki, T. Nagaya, H. Nagatomo, and K. Mima, Phys. Rev. Lett. **84**, 5331 (2000).
[9] A. L. Velikovich, A. J. Schmitt, J. H. Gardner, and N. Metzler, Phys. Plasmas **8**, 592 (2001).
[10] Y. Aglitskiy, A. L. Velikovich, M. Karasik, V. Serlin, C. J. Pawley, A. J. Schmitt, S. P. Obenschain, A. N. Mostovych, J. H. Gardner, and N. Metzler, Phys. Rev. Lett. **87**, 265002 (2001); Phys. Plasmas **9**, 2264 (2002).
[11] Wolfram Functions Site, http://functions.wolfram.com/HypergeometricFunctions/HypergeometricPFO/06/02/02/ see also A. P. Prudnikov, Yu. A. Brychkov, and O. I. Marichev, *Integrals and Series, Vol. 3: More Special Functions* (Gordon and Breach, New York, 1989).
[12] *Handbook of Mathematical Functions with Formulas, Graphs, and Mathematical Tables*, edited by M. Abramowitz and I. A. Stegun (National Bureau of Standards, U.S. Government Printing Office, Washington, DC, 1972).
[13] I. S. Gradshteyn and I. M. Ryzhik, *Tables of Integrals, Series and Products* (Academic Press, San Diego, 1994).
[14] N. Metzler, A. L. Velikovich, and J. H. Gardner, Phys. Plasmas **6**, 3283 (1999).
[15] A. L. Velikovich, A. J. Schmitt, N. Metzler, and J. H. Gardner, Phys. Plasmas **10**, 3270 (2003).
[16] D. Ryu and E. T. Vishniac, Astrophys. J. **313**, 820 (1987).
[17] J. M. Laming and J. Grun, Phys. Rev. Lett. **89**, 125002 (2002).
[18] L. I. Sedov, *Similarity and Dimensional Methods in Mechanics* (Academic, New York, 1959).
[19] L. D. Landau and E. M. Lifshitz, *Fluid Mechanics* (Pergamon, New York, 1987).
[20] J. P. Boris and D. L. Book, J. Comput. Phys. **11**, 38 (1973); also see *Solution of the Continuity Equation by the Method of Flux-Corrected Transport, Methods in Computational Physics* (Academic, New York, 1976), Vol. 16, pp. 85–129.
[21] S. T. Zalesak, A. J. Schmitt, J. H. Gardner, and A. L. Velikovich, Phys. Plasmas **12**, 056311 (2005).